Highlights of Vehicles

ISSN 2696-8347, A Peer-Reviewed Open Access Journal by Highlights of Science

https://www.hos.pub/ho/vehicles

Measuring Cyclist's Inputs, the Kinematic and Dynamic Properties of a City Bicycle, and Estimating the Road Profile via Sensor Fusion

by Murad Shoman, Hocine Imine, Kenth Johansson and Viveca Wallqvist

Cite this Article

Shoman, M., Imine, H., Johansson, K., & Wallqvist, V. (2023). Measuring Cyclist's Inputs, the Kinematic and Dynamic Properties of a City Bicycle, and Estimating the Road Profile via Sensor Fusion. *Highlights of Vehicles*, *1*(1), 1–16. https://doi.org/10.54175/hveh1010001

Highlights of Science

Publisher of Peer-Reviewed Open Access Journals

https://www.hos.pub

Barcelona, Spain

Article

Measuring Cyclist's Inputs, the Kinematic and Dynamic Properties of a City Bicycle, and Estimating the Road Profile via Sensor Fusion

Murad Shoman [1,*], **Hocine Imine** [1], **Kenth Johansson** [2] and **Viveca Wallqvist** [2]

[1] Laboratoire Perceptions, Interactions, Comportements Simulations des usagers de la route et de la rue (PICS-L), Components and Systems Department (COSYS), Gustave Eiffel University, Champs sur Marne 77420, France
[2] Division of Bioeconomy and Health, Department of Material and Surface Design, RISE Research Institutes of Sweden, Stockholm SE-114 28, Sweden
* For correspondence: murad.shoman@univ-eiffel.fr

Abstract In this paper, we present the instrumentation of a city bicycle with different sensors and devices in order to measure cyclists' inputs (i.e., pedaling and steering) and the dynamical and kinematic properties of the bicycle. The instrumentation includes two tri-axial accelerometers, an Inertial Measurement Unit (IMU), GPS, a potentiometer, a laser scanner, a pedaling power meter, and speed and cadence sensors, in addition to a mobile eye tracker worn by the cyclists. After the instrumentation and adjustment of the sensors, a study was conducted in the city of Stockholm using the instrumented bicycle with the aim to evaluate cycling safety and comfort on snowy surface conditions. The outputs of this experiment will be employed further to study the interaction of cyclists with road infrastructure and other road users and their impact on cyclists' behavior and cycling safety.

Keywords instrumented bicycle; on-road experiment; signal processing; cycling safety

1. Introduction

Cycling started to gain popularity among transportation stakeholders as one of the most sustainable modes of transportation for short and medium distances; new cycling modes are becoming more popular such as E-bikes and Bike-sharing services. This is because cycling is quiet, clean, takes up minimal area, provides regular physical activity, requires little infrastructure investment, cost-effective and quick means of transportation [1,2].

For example, in the USA, the number of cycling trips increased from 1.7 billion trips in 2004 to 4 billion trips in 2009 [3]. On the other side, cycling accidents increased; more than 1.35 million fatalities are reported worldwide every year, and as many as 50 million cyclists are being injured [4]. These accidents result from one or a combination of three main factors: infrastructure design and maintenance, vehicle condition, and users' behavior [5,6]. A study in Portland (US) ([7]) reported that nearly one in five cyclists experienced an event leading to injury, regardless of gender, age, body mass index (BMI), or cycling skill level, injuries were mainly caused by "slipping" (35%) or "collision with a car" (19%). In France, in 2021, 227 cyclists were killed, with a +21% increase compared to 2019. 31% of the accidents that caused deaths resulted from self-accidents [8].

The use of sensors and instrumentation in cycling is becoming increasingly popular and this technology is being used to improve performance and safety. The main goals of bicycle instrumentation include determining the trajectory classes for cyclists, collecting naturalistic cycling data, studying the bicycle's dynamics, and studying cyclists' behaviors. As technology continues to advance, it is likely that we will see even more sophisticated and innovative bicycle instrumentation in the future. Bicycle instrumentation typically includes a variety of sensors that measure speed, distance, cadence (pedaling rate), power output, heart rate, GPS location, and elevation.

One study found that the most common types of sensors used in cycling include speed, distance, and cadence sensors. These sensors can be used to provide real-time feedback to the rider, as well as to record data for later analysis. The authors also note that power meters, which measure the rider's output in watts, have become increasingly popular in recent years, especially among competitive cyclists [9].

Received: 16 November 2022
Accepted: 1 February 2023
Published: 5 February 2023

Academic Editor
Haiping Du, University of Wollongong, Australia

In London, the researchers instrumented a bicycle with a gyroscope, accelerometer, absolute encoder, and Hall Effect sensors to determine the trajectory for cyclists [10]. In another study the researchers used an instrumented bicycle to validate multibody modeling and simulation, the bicycle was equipped with five sensors, all connected with an Arduino board: an inertial measurement unit (IMU), an inclinometer, and incremental rotary encoders [11,12]. In [13] the researchers used a bicycle equipped with GPS, video camera, accelerometer, compass, and gyroscope to discover and characterize conflict points between cyclists and other road users. In [14] an instrumented bicycle was used to study the relation between bicycle ride quality and conventional pavement roughness. Another research focused on the turning behavior of cyclists by measuring steering torque and angle, and bicycle speed, acceleration, and angular velocity [15,16], whereas in [17] the hard breaking behavior was studied by analyzing speed and acceleration signals and detecting the abnormal signals after applying signal processing techniques. In another research, cycling safety was assessed from objective and perceived points of view, where the risk classification of the roadway components was compared [18].

In Gothenburg, Sweden, an instrumented bicycle was used to collect naturalistic cycling data, using two cameras (one facing forward and the other facing the cyclist's face), a GPS, two inertial measurement units (IMU), two pressure brake sensors, a speed sensor, and a push-button, to allow the cyclist to report any risks [19]. The findings reveal that cycling near crossings increases the danger, particularly when there is sight blockage (e.g., buildings and hedges), whereas poor maintenance and road surface condition raised the risk by ten times [20,21]. [22,23] studied the effect of the appearance of cyclists on drivers' overtaking proximities. It was found that overtaking distance decreases when vehicles pass a male cyclist, a cyclist wearing a helmet, or a cyclist cycling away from the road's edge. Whereas in [24] the results show that the passing distance decreased when motorcycles overtake a cyclist compared to cars and small trucks. Furthermore, cyclists appeared unstable when a bus (longer passing time) passed them. Another study by [25] shows that vehicle drivers do not provide a comfortable passing distance to cyclists in the adjacent cycling lane.

In this paper, we present the instrumentation of a city bicycle in Stockholm, Sweden. The used sensors collect comprehensive dynamical and kinematical data of the bicycle with the six Degrees of Freedom (DoF) measurements, besides the inputs of the cyclists (i.e., pedaling power and steering angle), and estimation of road profile input using the inertial method, which is applied for the first time using a bicycle. The gathering of the inputs/outputs of the bicycle-rider system allows us to understand better the connection between them to evaluate the effect of road infrastructure on bicycle stability and cyclist behavior objectively. The paper is structured as follows. The second section is devoted to describing the bicycle instrumentation; the third section describes the experimentation conducted in Stockholm city in Sweden; and the post signal processing and presents the output signals. We finalize with the conclusion and future work in the fourth section.

2. Bicycle Instrumentation Setup

We instrumented a bicycle with different sensors to detect the corresponding dynamical and kinematical data, as well as the road surface features. In addition, the cyclists wore eye-tracking glasses. The details about the used bicycle and sensors are shown below:

Bicycle: The bicycle used in this experiment is a Skeppshult Nova manufactured in Sweden equipped with Schwalbe Active Winter (Active Line, K-Guard) tires: 28" front and rear single-walled aluminum wheels with 36 spokes. The tires pressure was set to 4 bar (the recommended pressure is 2.0–5.0 bar). This bike supports a maximum weight of 100 kg (weight of the user + bike + luggage carried), the bicycle consists of a single-speed transmission system with a 5-speed shifter for ease of use. The total mass of the instrumented bicycle including the sensors and a laptop is 28 kg (the bicycle mass is 15.3 kg). The location of the instrumentation on the bicycle is detailed in the schematic in Figure 1 and described below.

1. **SG-LINK-200-OEM + Hall Effect Sensor** from Alliantech was used to count the number of rotations per minute (RPM) for the front wheel to calculate its angular velocity, the sensor was fixed on the front fork and connected to a 9V battery, and a magnet was attached to one of the spokes, each time the magnet passes the sensor it counts one rotation. The sampling rate was set to 250 Hz (adjustable up to 1024 Hz), and the data was logged remotely using WSDA 200 USB.

2. **G-link-200 Triaxial accelerometer** from AlianTeck is a wireless 3-axis accelerometer with ±2 to ±40 g measurement range, low noise waveform on all axes with 25 µg/Hz or 80 µg/Hz, the sampling rate is up to 4096 Hz, which was set to 500 Hz in this experiment. The sensor connects wirelessly to WSDA 200 USB to log the data. It was fixed on the front basket over the front wheel and used to measure the accelerations of the front part of the bicycle.
3. **GPS (Global Positioning System):** Edge 130 plus from Garmin that includes: GPS, GLONASS, and GALILEO systems to detect the position in real-time; barometric altimeter; accelerometer, and internal memory to save data from other Garmin devices such as Vector 3, speed and cadence sensors. The device was fixed on the handlebar in order to control it easily.
4. **P25 wire-wound potentiometer** from RS Pro: it is connected with specially designed cogs and attached to the handlebar to measure the steering angle, the potentiometer was adjusted to give 0° when the bicycle is pointing front, positive reading when turning right and negative when turning left. The potentiometer offers resistance up to 25 Ω with a temperature coefficient of ±50 ppm/°C, it includes a shaft of 6 mm diameter and provides 285° rotation (mechanical angle), with rotational life of up to 100,000 revolutions. The potentiometer is connected to Arduino microcontroller which allows logging the data using a serial portal connection on a laptop. The sampling rate is 100 Hz.

Figure 1. Schematic of the instrumented bicycle, more details about the different sensors following the correspondent numbers below.

5. **IMU unit+ WLAN "Shell" 4.0 Data Logger** from Avisaro, was used as a data logger with six DoF IMU units (three axes acceleration / three axes gyro), Built-in GPS Satellite Receiver and a slot for USB memory where the data are logged. The logger was fixed on the rear seat to measure the accelerations of the rear part of the bicycle and the rotations of the bicycle. It was aligned to the three axes of the bicycle. The IMU sampling rate was set to 100 Hz, and the measurement range for the accelerometer and gyrometer were set to ±2 g and 250 DPS respectively. The GPS receiver is installed internally avoiding the need for an external antenna, it has a position accuracy of 2.5 m in circular error probability (CEP) and a sampling rate of 1 Hz.

6. **OY1P303P0189 laser scanner** from Wenglor was used for the continuous measuring of the distance between the top of the rear seat and the road surface. The laser was fixed at the same level as the data logger and around 10 cm from the center of the rear wheel. The effective working range of the laser beam is 50–3050 mm, the measuring rate is 1–500 Hz, and the reproducibility is 1 mm maximum. The data are logged using the RS-232 interface connected through a serial portal to a computer. The sampling rate is 30 Hz.
7. **K2 power bank** from PowerOak was used as a battery to provide power to the laser scanner and the data logger. It has capacity of 185 Wh/50000 mAh with six output ports, one 20 V/5 A, one 12 V/2.5 A, two 5 V/2.1 A, and two 5 V/1 A with max power of 80 W. The dimensions of the battery are 20.6 × 13.5 × 3.3 cm and it weighs 1.26 kg.
8. **Speed sensor 2** from Garmin is a wireless sensor that gives longitudinal velocity and distance at all times with no magnets or other exposed parts. It was fixed on the hub of the rear wheel and self-calibrated with Edge 130 plus using Bluetooth. The wheel circumference was set to 2.15 m.
9. **Vector 3 power meter pedals** from Garmin provides dual-sensing on both pedals, each pedal weighs 316 g, and it bears a maximum rider weight of 105 kg with a measurement accuracy of +/− 1.0%.
10. **Cadence sensor 2** from Garmin was fastened to the left-side crank arm to measure pedal strokes per minute. It self-calibrates with Edge 130 plus using Bluetooth.
11. **WSDA 200 USB** from AlianTeck is a data acquisition gateway that collects synchronized data from scalable networks of wireless sensors such as G-link-200 and SG-link-200. It has a timestamp of ±50 µs in LXRS+ and LXRS-enabled modes, wireless range up to 2 km (400 m typical).
12. **Tobii Pro Glasses 2** from Tobii Pro were used to record the gaze of the participants in the experiment environment. The glasses allow data to be captured at 50 or 100 Hz and are connected to a recording unit where the data is saved on an SD card. The glasses contain a gyroscope and an accelerometer, four eye cameras, a scene camera with a resolution of 1920 × 1080 pixels at 25 fps, and a visual angle of 82° horizontal and 52° vertical, a microphone to record the ambient sounds and protective lenses.

The parameters of the fixed sensors were adjusted in order to get the desired measurements. The adjustment process included fixing the sensors in appropriate places on the bicycle, connecting them to the computer, choosing the most suitable sampling frequency and channel to log the data, and conducting tests to check if the output signals are coherent.

After the adjustment process finished, each cyclist was asked to ride the instrumented bicycle for around 3.5 km in Stockholm. Figure 2 shows the experiment's itinerary. The experiment was performed in February and the road surface condition was a mix between snow sludge and ice. The experimental route was classified into three zones: zone 1 has a length of 750 m and consists of a mixed traffic street with a 30 km/h speed limit, where the participant cycles on the carriageway alongside cars and other vehicles; zone 2 consists mainly of an on-street separate cycling lane without a physical barrier of 1.7 m width and 630 m long and a shared bicycle-bus lane of 370 m; zone 3 consists of a shared pedestrian-cyclists way that goes between trees and parking lots with a width of 5 m and length of 1 km. 22 cyclists were involved in the study, 14 male (M = 37.9, SD = ±13.4) and 8 female (M = 32.4, SD = ±14.1). They had an average cycling experience of 30.9 years (SD: ±15.9) for males and 26 years (SD: ±15.8) for females. The participants followed the predetermined route using a GPS map displayed on a mobile mounted on the handlebar.

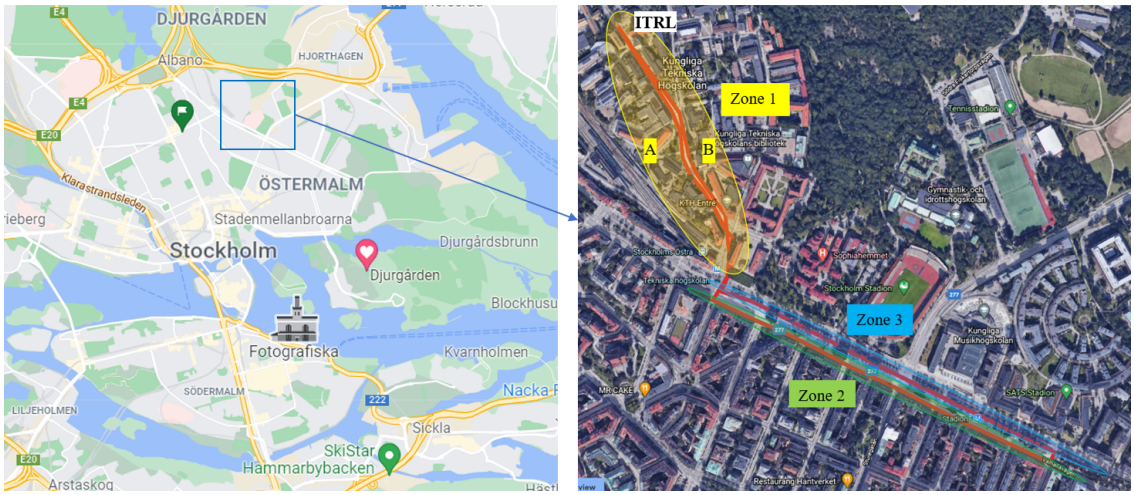

Figure 2. The location and the predetermined route of the experiment.

3. Signal Processing

After the experimentation, the signals from all sensors were collected and classified preparing for analysis. The total number of the output signals is 17, divided as follows: seven from the data logger (six from IMU and one from GPS), four from Aliantech sensors (G-link-200 and SG-link-200), one from the laser scanner, one from the potentiometer, and four from Garmin system. The output signals of the sensors were treated through multiple phases, as follows:

- Data synchronization: different acquisition systems were used as the sensors were not purchased from the same supplier, therefore, the synchronization of the output signals is essential to correlate between the measurements. The output signals started at different times, which generates a time lag that delicate the comparison between them. In order to remedy this and eliminate the lag effect, start point synchronization has been implemented by shifting the signal to be consistent with the last one to start. All signals were processed on MATLAB. The MATLAB code was designed to predict which signal started last (as the timestamp was recorded on the real-time HH:MM:SS:sss) and delete the collected data before this time for all the other signals, and then after applying the synchronization code the signals were compared to check if they start at the same time.
- Signal processing: to better exploit the measurements from the different sensors, a filtering process is necessary to remove the noise and extract the useful signal which will be analyzed later. In order to apply filters, we should know the frequency to estimate the power spectral density (PSD) of the signal using Welch's estimate method [26] to adjust the cut-off frequency. The PSD for most of the signals shows that their energy is concentrated on the frequencies between 0.3 and 30 Hz, hence, double filtering is necessary: a high pass filtering to remove the low frequencies caused by the low sensitivity of the sensor, and a low pass filtering to remove the high frequencies correspond to the noise. Different low and high pass filters were tested on the signal with different cut-off frequencies, Butterworth filter has been chosen as it gives the best calibration of the signal and removes the noise without negatively impacting the real signal. The cutoff frequencies were chosen depending on the frequency of the output signal (as different acquisition systems were used, the output signals had different frequencies), and the existence of the noise. For example, for the IMU output signals a low pass filter at a cutoff frequency of 20 Hz and a high pass filter at a cutoff frequency of 0.6 Hz were applied except for yaw rate output a low pass filter of 10 Hz was applied; for the SG-link-200 output signals a low pass filter at a cutoff frequency of 30 Hz and a high pass filter at a cutoff frequency 0.3 Hz were applied; for the laser scanner output signal a high pass filter at a cutoff frequency 0.6 Hz were applied; and for the potentiometer output signal, a low pass filter of 10 Hz was applied.

Figure 3 shows the filtration applied on the lateral acceleration of the rear wheel, the signal was extracted for the IMU unit. We can notice the noise removal from the original signal and the shape improvement, this becomes clearer when zooming at 639–644 s.

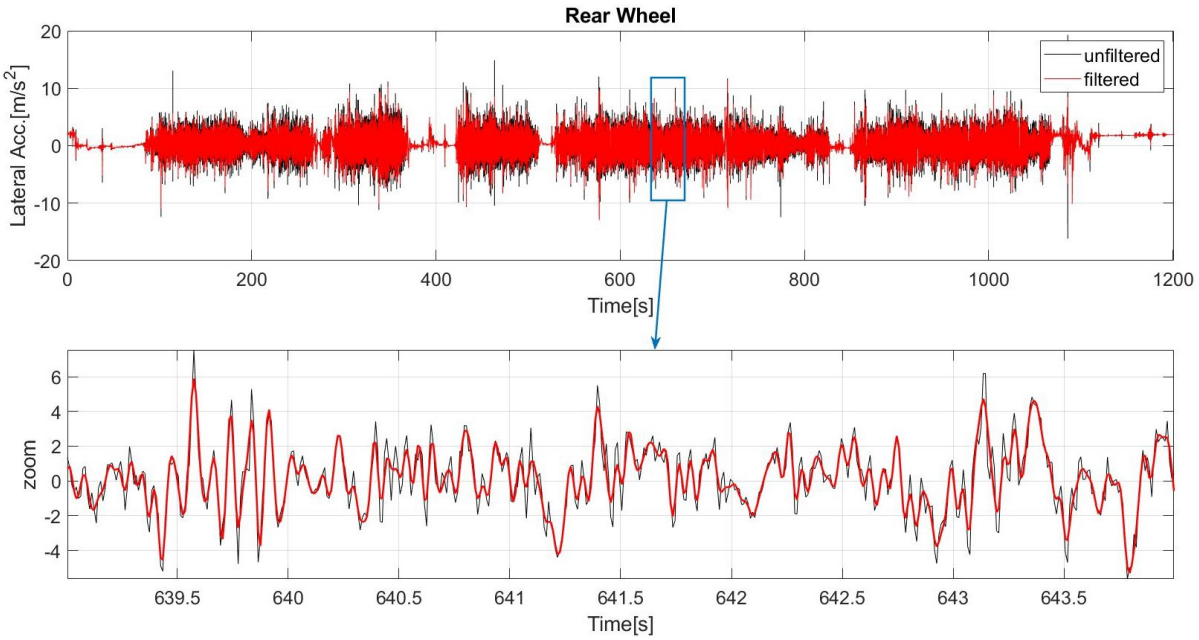

Figure 3. Comparison between "Unfiltered" and "Filtered" signals of the lateral acceleration measured using the IMU unit.

A. Trajectory and Position

The trajectory of one of the participants is shown in Figure 4. The participant followed exactly the predetermined route, even though the lateral position is inaccurate because of loss or weakness of the GPS signal. Figure 5 shows the altitude above sea level for the experimental route. We can notice that in zone 1A and zone 2 the route is mostly downhill, while in zone 3 and zone 1B, it is mostly uphill.

Figure 6 shows the X and Y positions for one of the participants, which were extracted from the east and north coordinates of the GPS. The change of position is clear at the beginning of zone 3 (525 s) where the cyclist had to make a U-turn. The GPS signal from 20 s to 120 s seems to be weak which affected the accuracy of the position measurement.

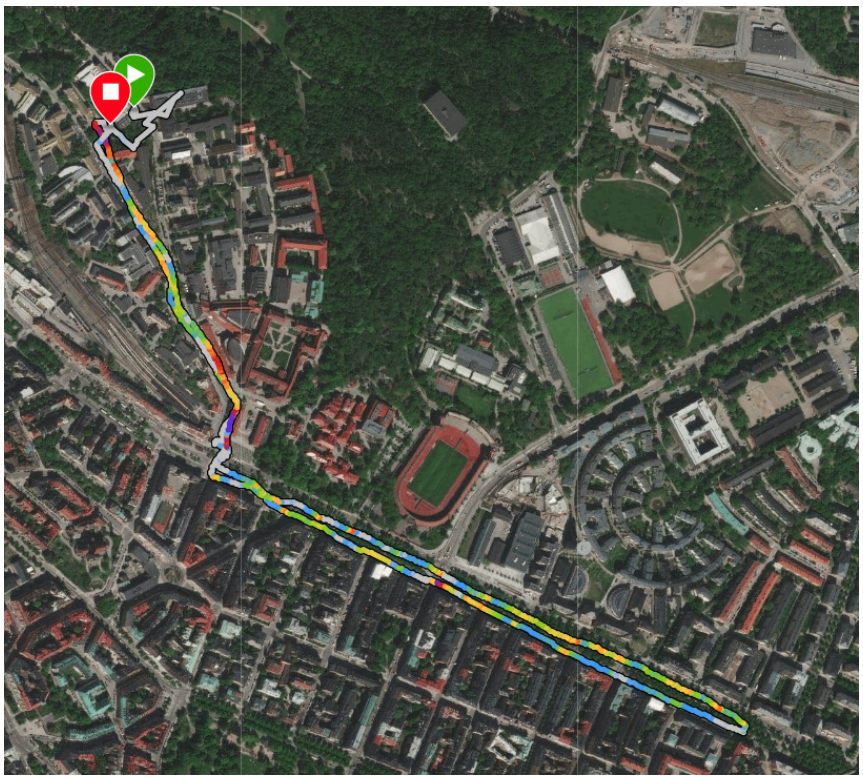

Figure 4. The experiment trajectory for a participant extracted from Edge 130 plus.

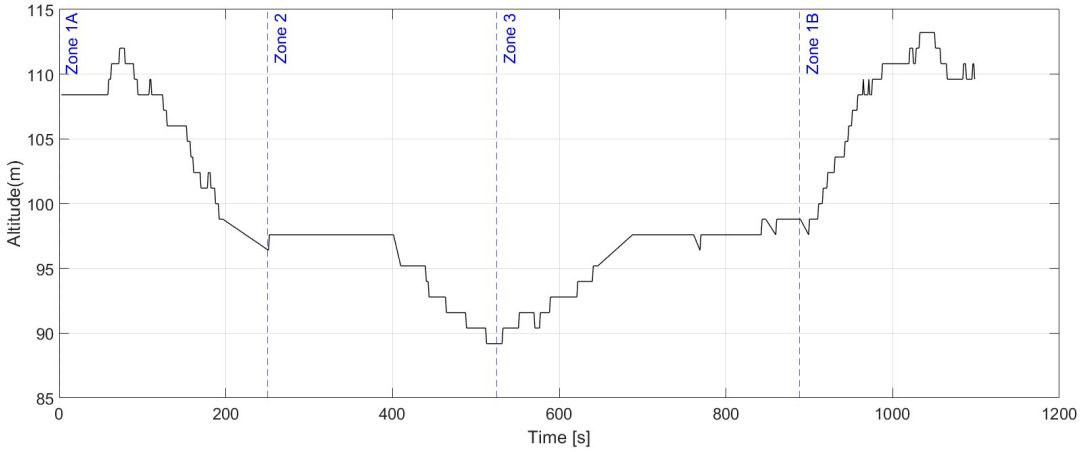

Figure 5. Elevation extracted from the GPS device fixed on the rear wheel.

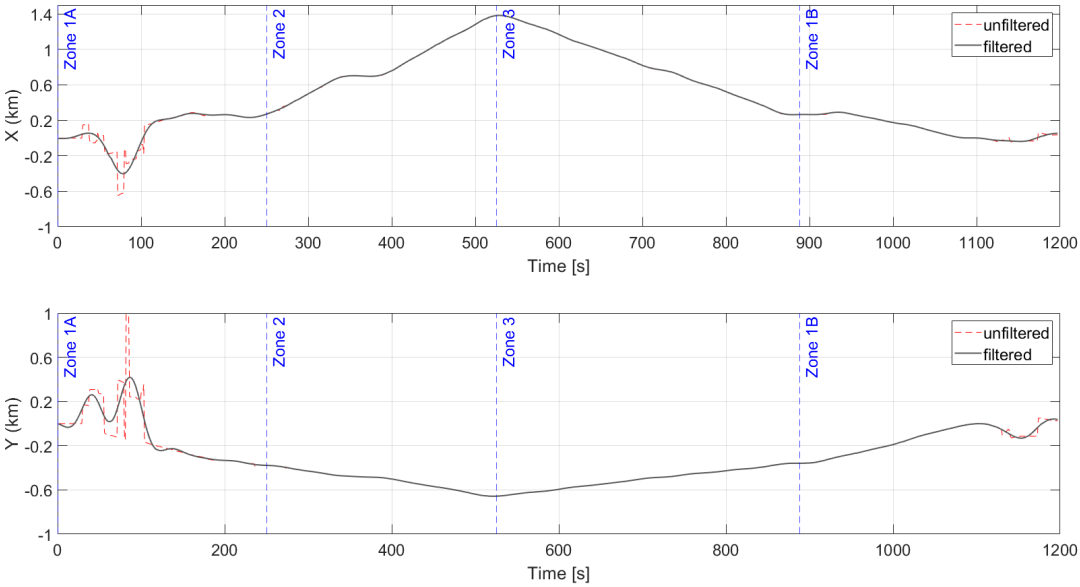

Figure 6. X and Y positions extracted from the GPS device fixed on the rear wheel.

B. Longitudinal Acceleration, Velocity, and Displacement

Figures 7 and 8 show the longitudinal acceleration (with zoom between 859–860 s), velocity, and displacement for the front and rear wheels respectively. The acceleration was filtered using the filtfilt method, which performs zero-phase digital filtering by processing the input data both forward and backward [27]. After applying the filter, the velocity was calculated by integrating the acceleration, the same filtering method was repeated after the calculation of the velocity in order to remove high frequencies, and finally, the displacement was calculated by double integrating the acceleration. We can notice the effect of filtering in noise removal and normalization of the signal.

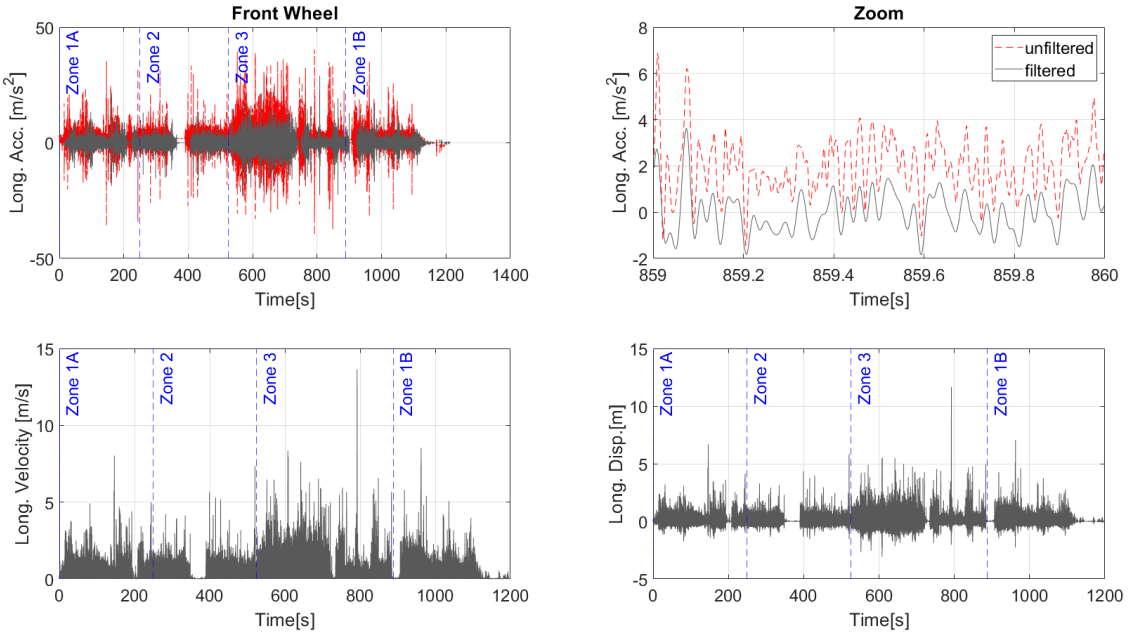

Figure 7. Longitudinal acceleration, velocity, and displacement were extracted from SG-Link-200 which was fixed on the front basket of the bicycle.

We can notice that both front and rear accelerations have negative values, despite the fact that the accelerometers were moving along the positive axis direction all the time during the experiment. To overcome this, the negative part of the signal was deleted before integrating for the velocity and displacement.

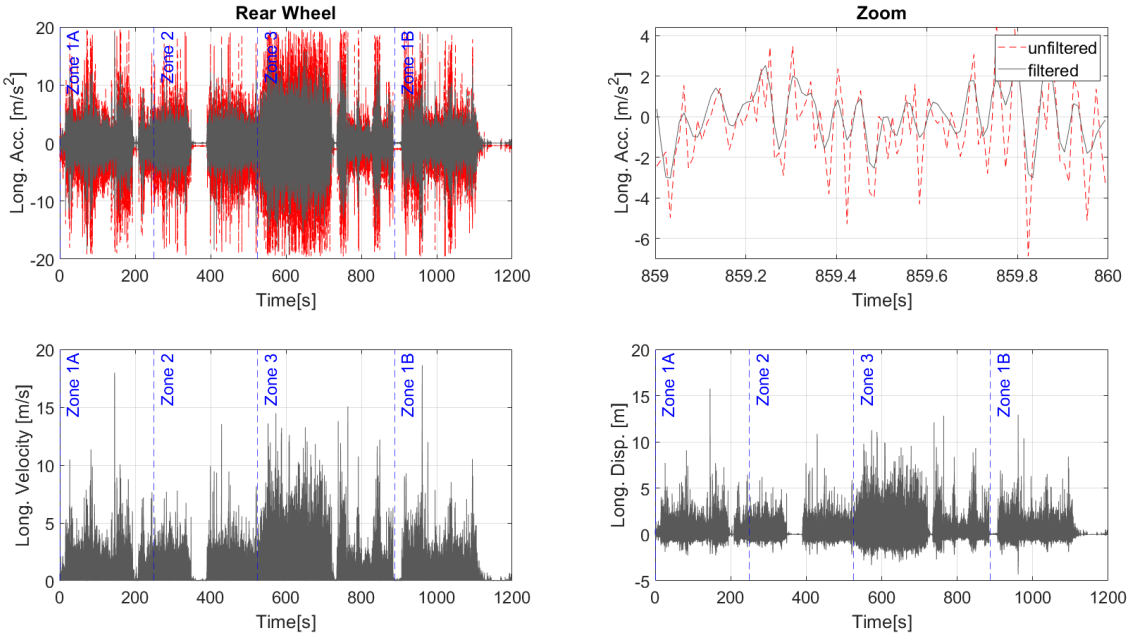

Figure 8. Longitudinal acceleration, velocity, and displacement were extracted from IMU which was fixed on the rear seat of the bicycle.

Figure 9 compares the speed profiles calculated using different output signals. Despite that all profiles show the same behavior, we can notice that the speed extracted from the IMU unit and SG-link-200 are still very noisy even after the filtration; whereas the speed coming from G-link-200 (which was calculated using Equation (1)) shows time delay and perturbations due to the fixation method of the sensor- it consisted of two separate parts, which could have moved during the experiment affecting the accuracy of the collected data. As a result, the speed extracted from the Garmin speed sensor was chosen to be the most accurate as it is well-filtered and has no perturbations.

$$v = \frac{RPM}{60} 2\pi r_e \tag{1}$$

where v is the equivalent longitudinal velocity, RPM is the number of rotations per minute collected from the hall effect sensor, and r_e is the effective radius of the front wheel of the bicycle.

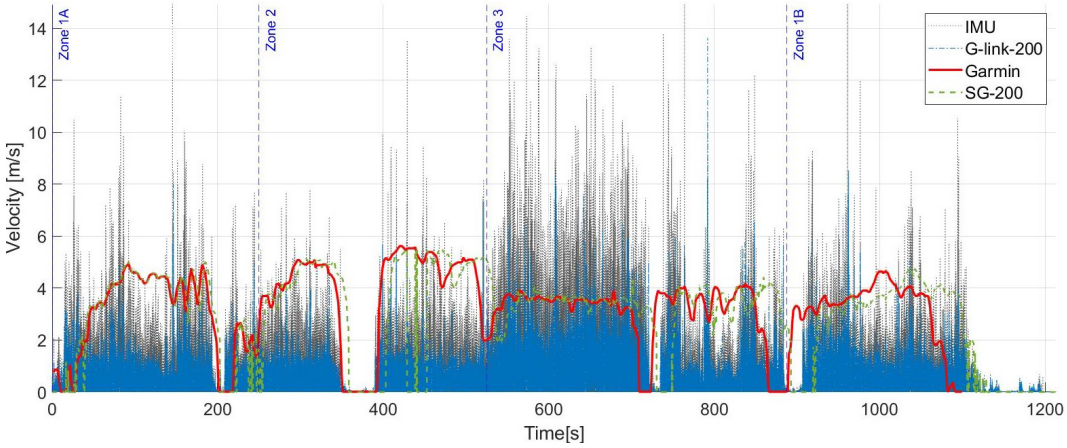

Figure 9. Comparison between velocities calculated using different sensors.

We can notice that the participant reached the maximum speed in zone 2 where there is a separate cycling lane, whereas he decreased his speed when cycling alongside pedestrians in zone 3.

C. Lateral Acceleration, Velocity, and Displacement

Figures 10 and 11 show the lateral acceleration (with zoom between 859–860 s), velocity, and displacement for the front and rear wheels respectively. The acceleration was filtered using the filtfilt method. After applying the filter, the velocity was calculated by integrating the acceleration, the same filtering method was repeated after the calculation of the velocity in order to remove high frequencies, and finally, the displacement was calculated by double integrating the acceleration. We can notice the effect of low pass filtering in noise removal and high pass filtering in the normalization of the signal. We can notice the increase in lateral acceleration and displacement in the first half of zone 3 despite the decrease in velocity in this zone, this could be explained by the maneuvers the cyclists had to make to pass pedestrians and the effect of the unevenness of the compacted soil surface on his stability.

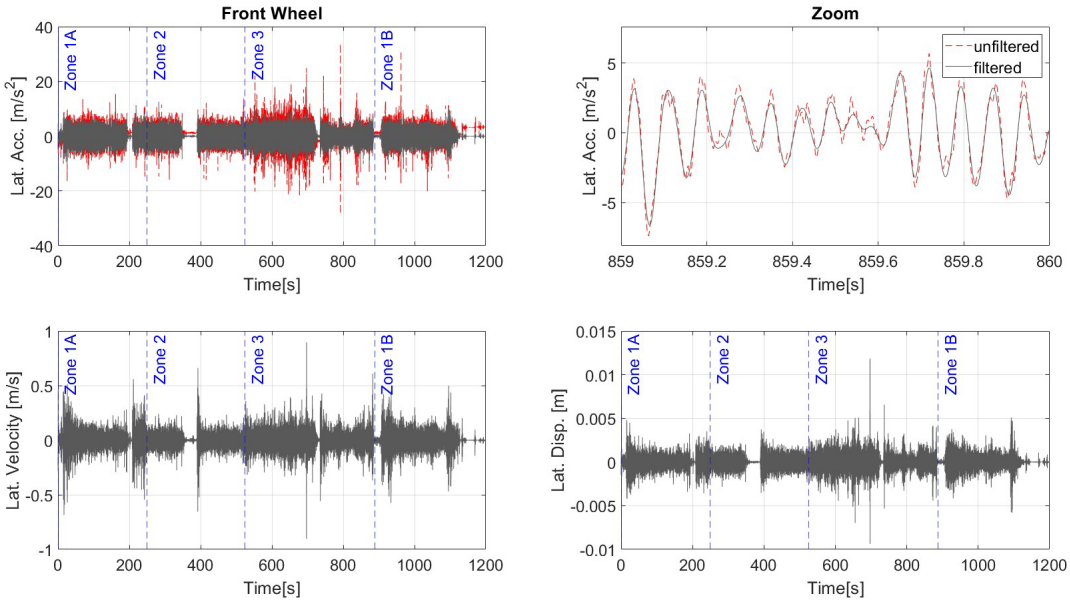

Figure 10. Lateral acceleration, velocity, and displacement were extracted from G-link-200 which was fixed on the front basket of the bicycle.

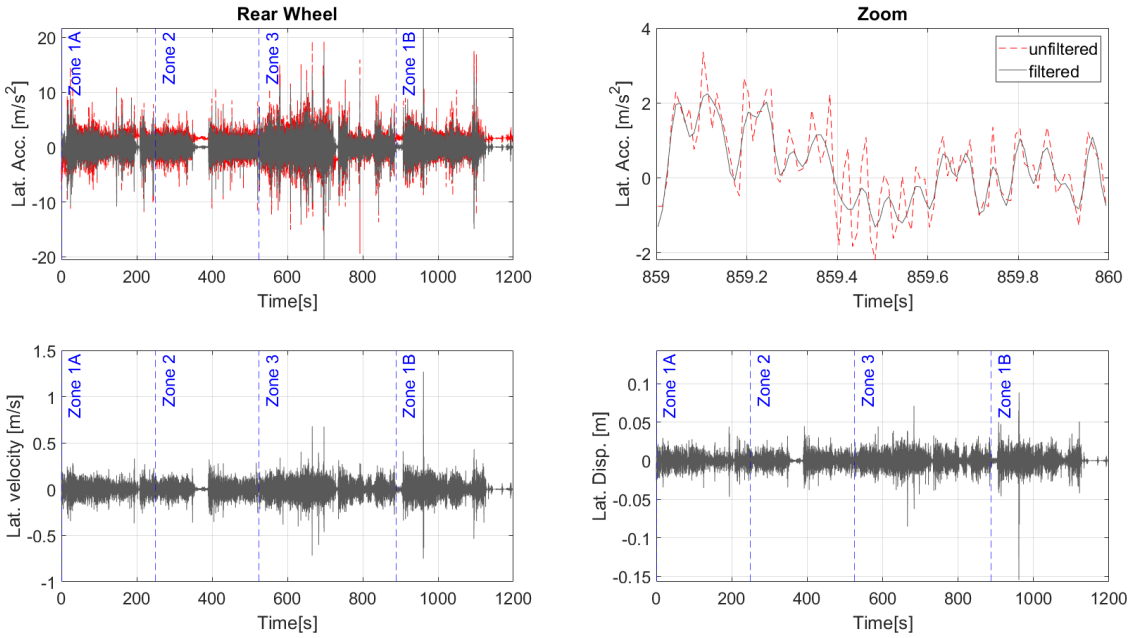

Figure 11. Lateral acceleration, velocity, and displacement were extracted from IMU which was fixed on the rear seat of the bicycle.

D. Vertical Acceleration, Velocity, and Displacement

Figures 12 and 13 show the vertical acceleration (with zoom between 859–860 s), velocity, and displacement for the front and rear wheels respectively. The acceleration was filtered using the filtfilt method. After applying the filter, the velocity was calculated by integrating the acceleration, the same filtering method was repeated after the calculation of the velocity in order to remove high frequencies, and finally, the displacement was calculated by double integrating the acceleration. We can notice the effect of low pass filtering in noise removal and high pass filtering in the normalization of the signal (where the gravitational acceleration was removed). For the rear wheel, the signal shows inaccuracy due to the limitation of the vertical accelerometer tolerance that was set to ±2 G.

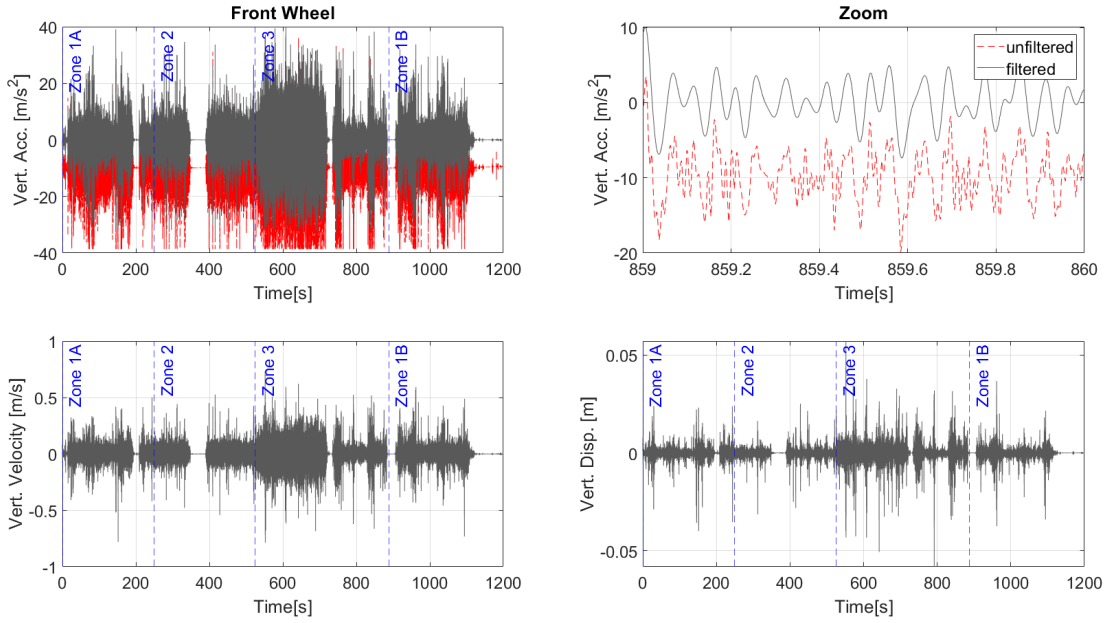

Figure 12. Vertical acceleration, velocity, and displacement were extracted from G-link-200 which was fixed on the front basket of the bicycle.

We can notice an increase in vertical acceleration in the first half of zone 3, where the surface is compacted soil, which affect the vertical stability of the bicycle.

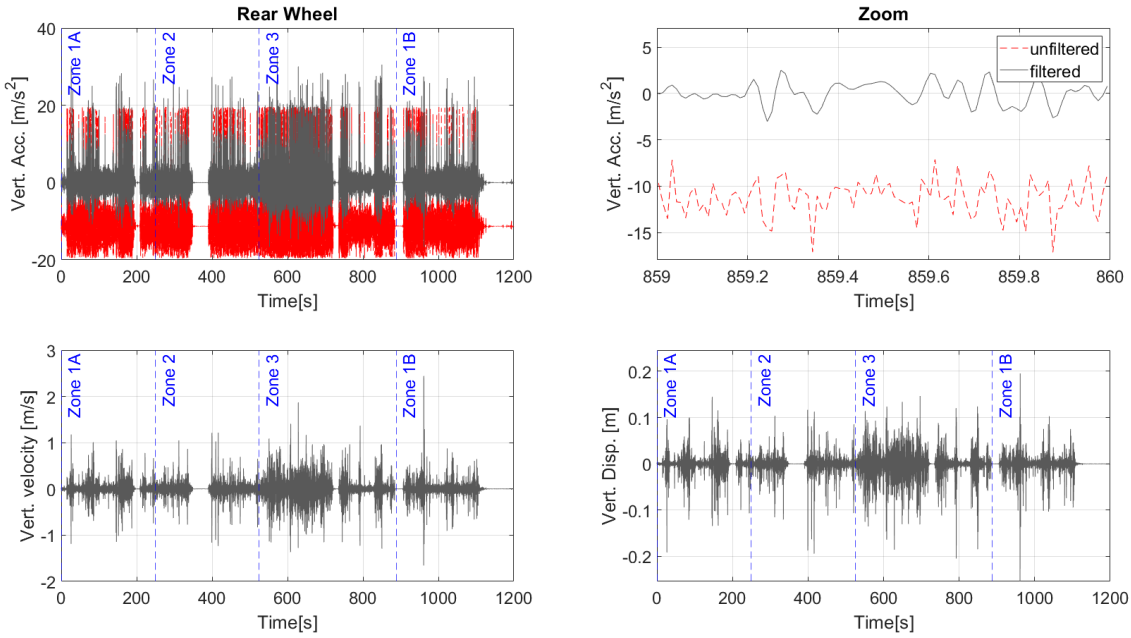

Figure 13. Vertical acceleration, velocity, and displacement extracted from IMU which was fixed on the rear seat of the bicycle.

Figure 14 shows the output of the laser scanner which is used to calculate the road profile using the inertial method [28,29] by applying Equation (2). In order to be able to calculate the road profile, the number of points collected by the accelerometer was reduced to match the number of points collected by the laser scanner (by keeping one point every three points iteratively). The deletion of these points reduced the accuracy of the calculated road profile. We can notice the perturbations of the laser scanner signal which leads to the increase of the amplitude of the road profile between 240 and 440 s, which mismatches the behavior of the vertical acceleration. This could be explained by the difference in the lateral position between the accelerometer and the laser scanner, which leads to measuring the vertical distance on two different spots. This impact becomes significant since the measurement took place on snowy surface condition, for example, if the wheel roll over a snow puddle, the vertical distance calculated using the accelerometer is to the top of the puddle while the laser scanner measures the distance to the bottom of it. We can notice at 670 s the perturbation in the laser scanner signal and it affects the calculation of road profile and, as a consequence, its effect on vertical displacement and vertical stability of the bicycle.

$$\mu = \iint \ddot{z} - s \tag{2}$$

where μ is the road profile, $\ddot{z}$ is the vertical acceleration output from G-link-200, and s is the distance between the laser scanner and the road surface.

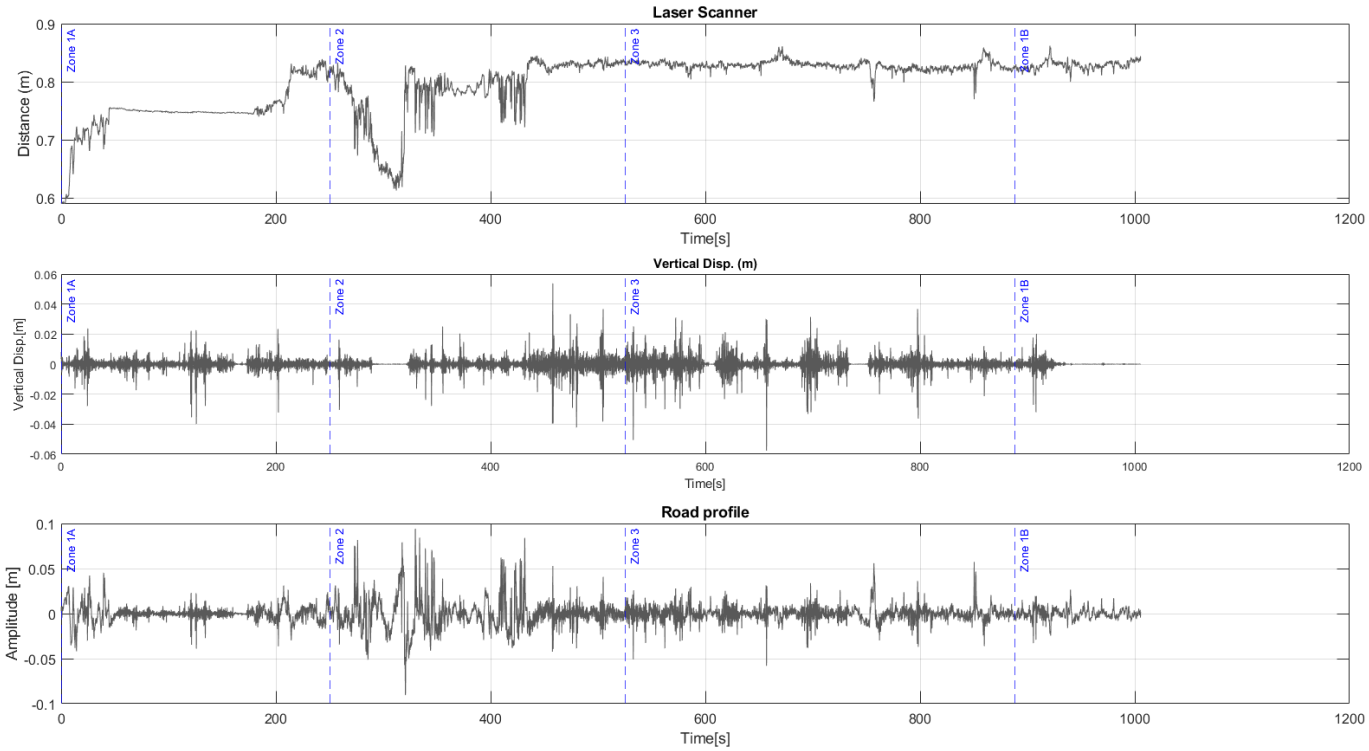

Figure 14. Calculated road profile.

E. Rotational Outputs

Figure 15 shows the steering angle extracted from the potentiometer attached to the handlebar, the signal was normalized and a low pass filter was used to remove the noise. The high value of the steering angle at the end (around 84°) represents the bicycle when it is stationary. It is noticed that the maximum value of steering while the bicycle is moving occurred when turning left on the intersection between zone 1A and zone 2—it is even higher than the U-turn between zone 2 and 3; looking at the map, we can notice that the degree of curvature is sharp (less than 90°) which explains the increase of the steering angle and the reduction in velocity.

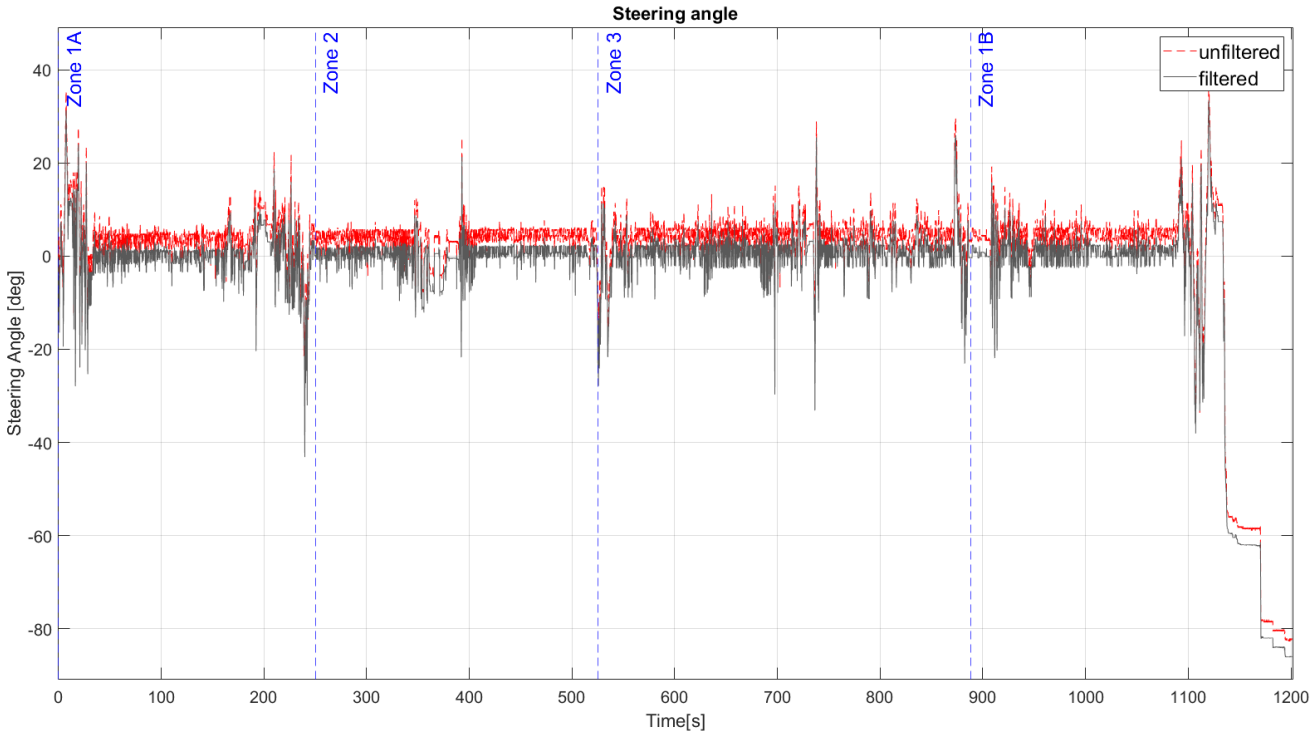

Figure 15. The steering angle was calculated using the data of the potentiometer, positive value indicates turning right, and negative turning left.

Figure 16 shows the pitch rate and angle which were calculated by integrating pitch rate over time. We can notice the increase of pitch rate and value when strongly accelerating or decelerating, this becomes clear at 395, 900, and 1130 s. It is also noticed that the pitch value increased reflecting the unevenness of the road profile, for example, around 700 s.

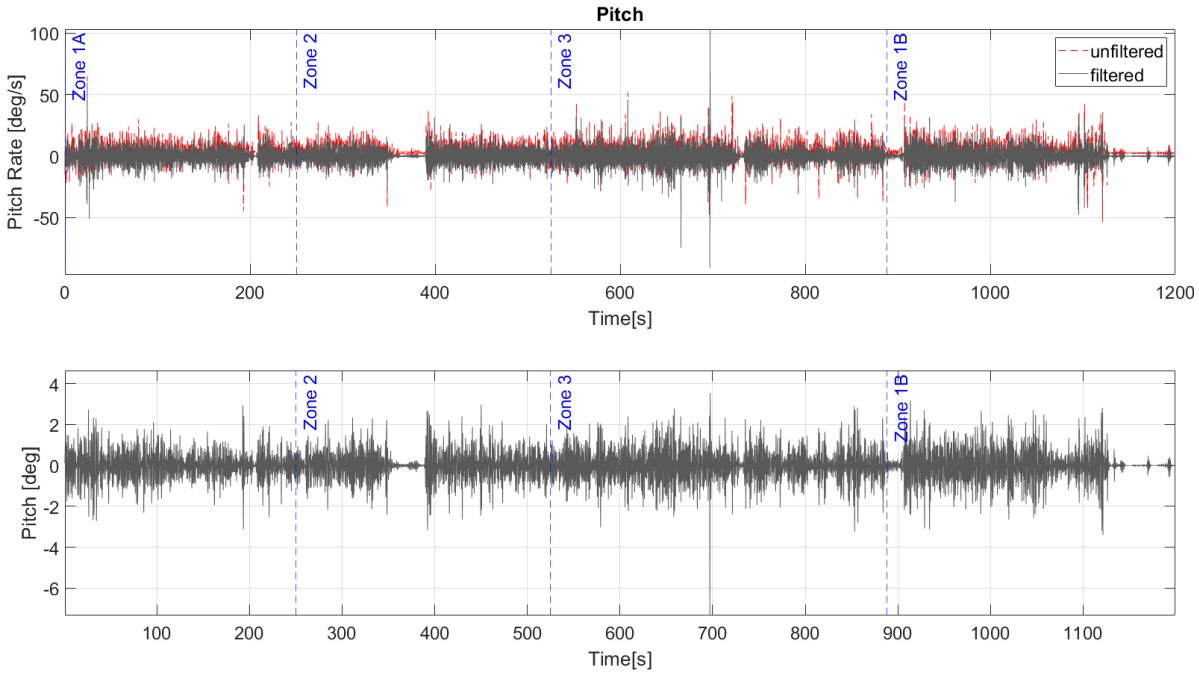

Figure 16. Pitch rate and angle extracted from IMU which was fixed on the rear seat of the bicycle.

Figure 17 shows the roll rate and angle calculated by integrating the roll rate over time. We can notice an increase in role rate and value in the first half of zone 3, without any significant change in steering angle for the same zone. This could be explained by the unevenness of the compacted soil surface and the maneuvers done by the cyclists to pass pedestrians, which could be an indication of compromised lateral stability.

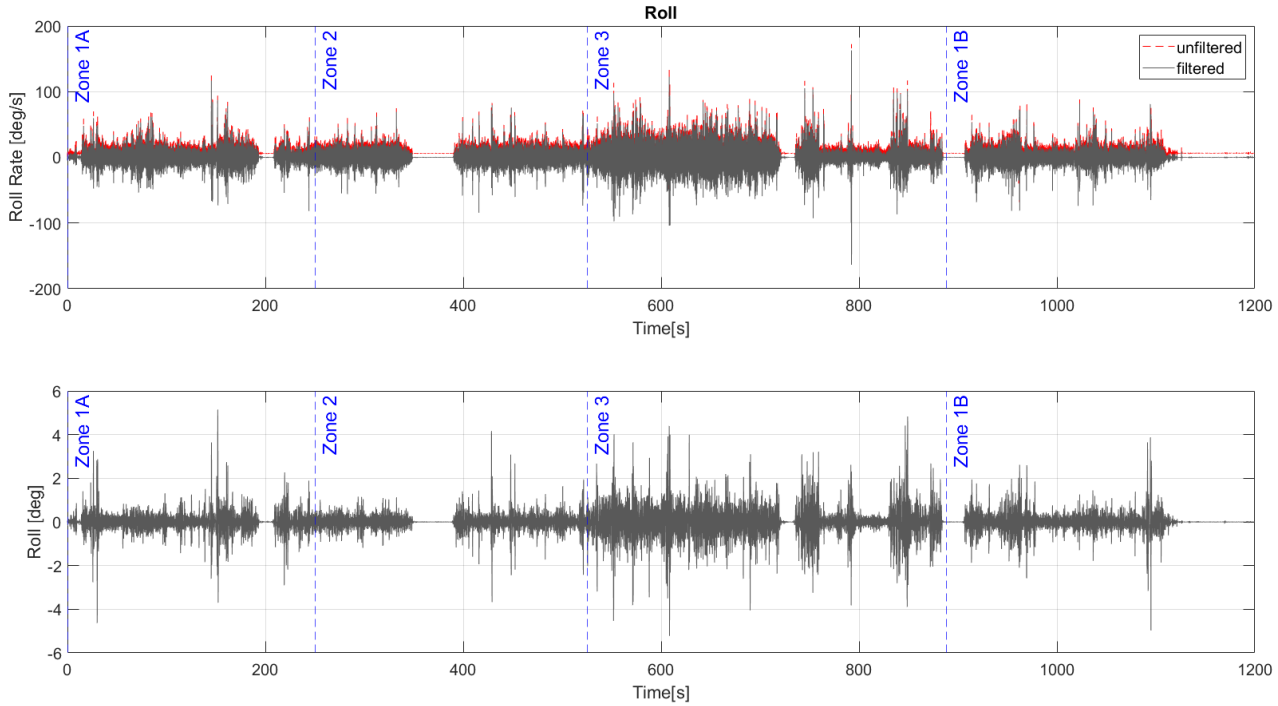

Figure 17. Roll rate and angle extracted from IMU which was fixed on the rear seat of the bicycle.

Figure 18 shows the yaw rate and angle, which were calculated by integrating the yaw rate over time. We can notice the increase in yaw rate and value when strongly accelerating or decelerating, this becomes clear at 395, 900, and 1130 s.

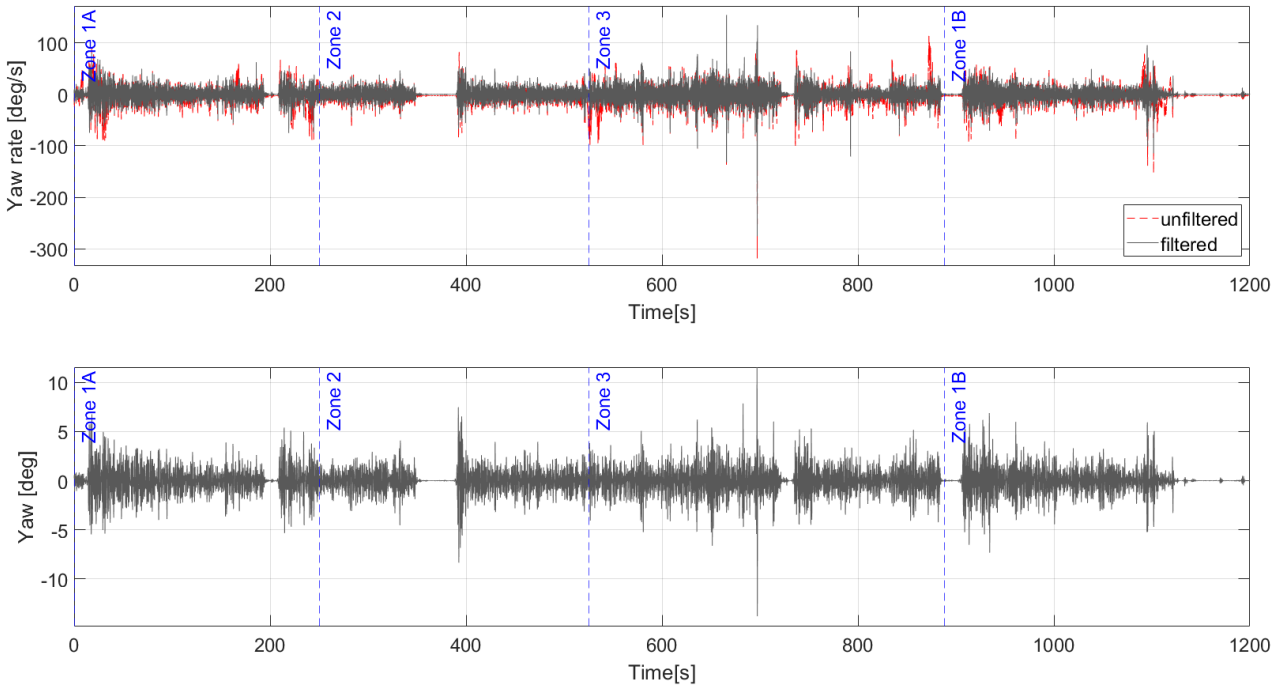

Figure 18. Yaw rate and angle extracted from IMU which was fixed on the rear seat of the bicycle.

F. Pedaling Power and Cadence

Figure 19 shows the pedaling power and cadence of one of the cyclists. It is noticed the maximum power was consumed in zone 1B according to the increased slope. Compared to the speed profile there was a speed decrease in this area. We can also notice that the cyclist tends to increase the power to maintain a steady cadence, for example when he consumed the maximum power in zone 1B. The increase of power without reflecting on cadence and speed indicates the wheel is slipping over the road surface.

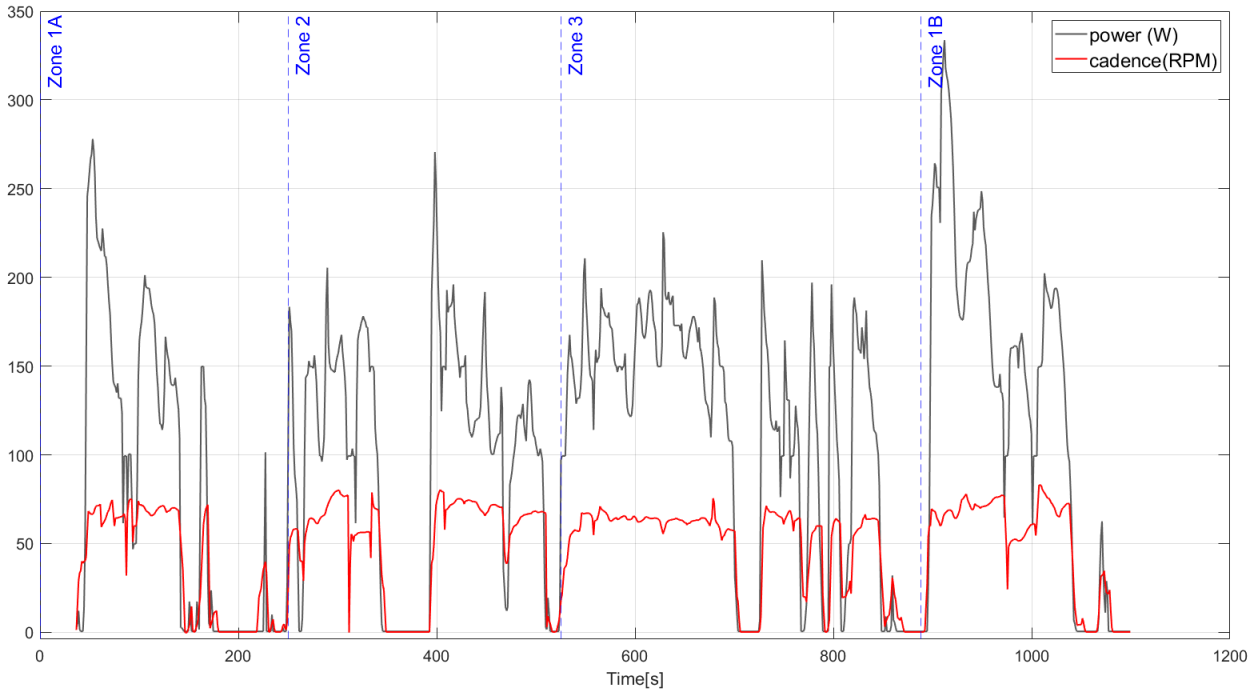

Figure 19. Pedaling power and cadence.

The pedaling cadence is not always proportional to the speed, for example, around 400 s the cadence peaks whereas the speed peaks after 20 s.

4. Conclusion

In this paper, we presented our work on bicycle instrumentation and the subsequent experimentation and processing of the output signals. The instrumented bicycle was equipped with sensors measuring the bicycle's kinematical and dynamical properties while taking into account all six degrees of freedom (longitudinal, lateral, vertical, Yaw, Pitch, and Roll). The following sensors were included: a tri-axial accelerometer, an Inertial Measurement Unit (IMU), a GPS, a potentiometer, a laser scanner, a pedaling power meter, and speed and cadence sensors. The inputs (such as steering angle and pedaling cadence) and outputs (such as the six DoFs, speed, and position) of the system were measured and logged. The collected data were then processed on MATLAB, first by synchronizing all signals as different acquisition systems were used and then by testing different filtration techniques and choosing the most suitable one to remove the noise and normalize signals.

A sample of all input and output signals was then presented to one of the participants. The comparison between signals before and after processing shows the impact of filtration in noise removal without negatively impacting the utilizable signals. The same process was then applied to the output signals for the 22 cyclists who participated in the experiment. The reliability of processed signals allows us to study the connection between the inputs and outputs of the system and their impact on cycling behavior and safety.

In future work, the detailed analysis of all signals for all participants, the experimentation results, the answers to the subsequent questionnaire, and the eye-tracker videos will be investigated in order to study the behavior of the cyclists and the effect of road surface characteristics and geometries on safer user behavior. The measured parameters will be compared to the outputs of the PICS-L bicycle simulator [30–32] where the same experiment scenario was reproduced in order to validate the underlying mathematical model.

Funding

This work is funded by Marie Skłodowska-Curie actions (H2020 MGA MSCA-ITN) within the SAFERUP project under grant agreement number 765057.

Data Availability

The data used to support the findings of this paper are available from the corresponding author upon request.

Acknowledgments

The authors gratefully acknowledge the contribution of the Integrated Transport Research Lab (ITRL) at the Royal Institute of Technology (KTH) represented by Eng. Chirag Savant for hosting a part of this research.

Author Contributions

Conceptualization: M.S., & H.I.; Methodology: M.S., & H.I.; Software: M.S., & H.I.; Validation: M.S., & H.I.; Formal analysis: M.S.; Investigation: M.S.; Resources: M.S., K.J., V.W., & H.I.; Data curation: M.S.; Supervision: K.J., V.W., & H.I.; Writing – original draft preparation: M.S.; Writing – review and editing: K.J., V.W., & H.I. All authors have read and agreed to the published version of the manuscript.

Conflicts of Interest

The authors have no conflict of interest to declare.

References

1. Götschi, T., Garrard, J., & Giles-Corti, B. (2016). Cycling as a part of daily life: A review of health perspectives. *Transport Reviews*, *36*(1), 45–71. https://doi.org/10.1080/01441647.2015.1057877
2. Raser, E., Gaupp-Berghausen, M., Dons, E., Anaya-Boig, E., Avila-Palencia, I., Brand, C., et al. (2018). European cyclists' travel behavior: differences and similarities between seven European (PASTA) cities. *Journal of Transport & Health*, *9*, 244–252. https://doi.org/10.1016/j.jth.2018.02.006

3. Pucher, J., Buehler, R., Merom, D., & Bauman, A. (2011). Walking and cycling in the United States, 2001–2009: Evidence from the national household travel surveys. *American Journal of Public Health*, *101*(no. S1), S310–S317. https://doi.org/10.2105/AJPH.2010.300067
4. World Health Organization. (2018). *Global status report on road safety 2018*. World Health Organization.
5. Bucchi, A., Sangiorgi, C., & Vignali, V. (2012). Traffic psychology and driver behavior. *Procedia - Social and Behavioral Sciences*, *53*, 972–979. https://doi.org/10.1016/j.sbspro.2012.09.946
6. Shoman, M., Simone, A., & Vignali, V. (2018). Looking behavior to vertical road signs on rural roads. *MOJ Civil Engineering*, *4*(2), 75–79. https://doi.org/10.15406/mojce.2018.04.00100
7. Hoffman, M. R., Lambert, W. E., Peck, E. G., & Mayberry, J. C. (2010). Bicycle commuter injury prevention: it is time to focus on the environment. *The Journal of Trauma: Injury, Infection, and Critical Care*, *69*(5), 1112–1119. https://doi.org/10.1097/TA.0b013e3181f990a1
8. Observatoire national Interministériel de la sécurité routière. (2021). *La sécurité routière en France Bilan de l'accidentalité de l'année 202*1 (in Franch). Observatoire national Interministériel de la sécurité routière.
9. Gadsby A., &. Watkins, K. (2020). Instrumented bikes and their use in studies on transportation behaviour, safety, and maintenance. *Transport Reviews*, *40*(6), 774–795. https://doi.org/10.1080/01441647.2020.1769227
10. Miah, S., Milonidis, E., Kaparias, I., & Karcanias, N. (2019). An innovative multi-sensor fusion algorithm to enhance positioning accuracy of an instrumented bicycle. *IEEE Transactions on Intelligent Transportation Systems*, *21*(3), 1145–1153. https://doi.org/10.1109/TITS.2019.2902797
11. Escalona, J. L., & Recuero, A. M. (2012). A bicycle model for education in multibody dynamics and real-time interactive simulation. *Multibody System Dynamics*, *27*, 383–402. https://doi.org/10.1007/s11044-011-9282-7
12. Escalona, J. L., Kłodowski, A., & Munoz, S. (2018). Validation of multibody modeling and simulation using an instrumented bicycle: from the computer to the road. *Multibody System Dynamics*, *43*, 297–319. https://doi.org/10.1007/s11044-018-9626-7
13. Etemad, H., Costello, S. B., Wilson, D. J., & Padiyara, S. (2016). Using an instrumented bicycle to help understand cyclists' perception of risk. *Road & Transport Research*, *25*(3), 75–78.
14. Qian, X., Moore, J. K., & Niemeier, D. (2020). Predicting bicycle pavement ride quality: Sensor-based statistical model. *Journal of Infrastructure Systems*, *26*(3), 04020033. https://doi.org/10.1061/(ASCE)IS.1943-555X.0000571
15. Cain, S. M., & Perkins, N. C. (2012). Comparison of experimental data to a model for bicycle steady-state turning. *Vehicle System Dynamics*, *50*(8), 1341–1364. https://doi.org/10.1080/00423114.2011.650181
16. Dialynas, G., Christoforidis, C., Happee, R., & Schwab, A. (2023). Rider control identification in cycling taking into account steering torque feedback and sensory delays. *Vehicle System Dynamics*, *61*(1), 200–224. https://doi.org/10.1080/00423114.2022.2048865
17. Murgano, E., Caponetto, R., Pappalardo, G., Cafiso, S. D., & Severino, A. (2021). A novel acceleration signal processing procedure for cycling safety assessment. *Sensors*, *21*(12), 4183. https://doi.org/10.3390/s21124183
18. Cafiso, S., Pappalardo, G., & Stamatiadis, N. (2021). Observed risk and user perception of road infrastructure safety assessment for cycling mobility. *Infrastructures*, *6*(11), 154. https://doi.org/10.3390/infrastructures6110154
19. Dozza, M., Werneke, J., & Fernandez, A. (7–8 November 2012). *Piloting the naturalistic methodology on bicycles*. International Cycling Safety Conference, Helmond, The Netherlands.
20. Dozza, M., & Werneke, J. (2014). Introducing naturalistic cycling data: What factors influence bicyclists' safety in the real world? *Transportation Research Part F: Traffic Psychology and Behaviour*, *24*, 83–91. https://doi.org/10.1016/j.trf.2014.04.001
21. Dozza, M., Piccinini, G. F. B., & Werneke, J. (2016). Using naturalistic data to assess e-cyclist behavior. *Transportation Research Part F: Traffic Psychology and Behaviour*, *41*(Part B), 217–226. https://doi.org/10.1016/j.trf.2015.04.003
22. Walker, I. (2007). Drivers overtaking bicyclists: Objective data on the effects of riding position, helmet use, vehicle type and apparent gender. *Accident Analysis & Prevention*, *39*(2), 417–425. https://doi.org/10.1016/j.aap.2006.08.010
23. Walker, I., Garrard, I., & Jowitt, F. (2014). The influence of a bicycle commuter's appearance on drivers' overtaking proximities: An on-road test of bicyclist stereotypes, high-visibility clothing and safety aids in the united kingdom. *Accident Analysis & Prevention*, *64*, 69–77. https://doi.org/10.1016/j.aap.2013.11.007
24. Chuang, K.-H., Hsu, C.-C., Lai, C.-H., Doong, J.-L., & Jeng, M.-C. (2013). The use of a quasi-naturalistic riding method to investigate bicyclists' behaviors when motorists pass. *Accident Analysis & Prevention*, *56*, 32–41. https://doi.org/10.1016/j.aap.2013.03.029
25. Parkin, J., Wardman, M., & Page, M. (2008). Estimation of the determinants of bicycle mode share for the journey to work using census data. *Transportation*, *35*, 93–109. https://doi.org/10.1007/s11116-007-9137-5
26. Welch, P. (1967). The use of fast fourier transform for the estimation of power spectra: A method based on time averaging over short, modified periodograms. *IEEE Transactions on Audio Electroacoustics*, *15*(2), 70–73. https://doi.org/10.1109/TAU.1967.1161901
27. Gustafsson, F. (1996). Determining the initial states in forward-backward filtering. *IEEE Transactions on Signal Processing*, *44*(4), 988–992. https://doi.org/10.1109/78.492552
28. Imine, H. (2003). *Observation d'états d'un véhicule pour l'estimation du profil dans les traces de roulement* (in Franch) [PhD thesis, Versailles-St Quentin en Yvelines]. ABES. https://www.theses.fr/2003VERS0026
29. Imine, H., Fridman, L., Shraim, H., & Djemai, M. (2011). *Sliding mode based analysis and identification of vehicle dynamics* (Vol. 414). Springer Science & Business Media.
30. Shoman, M., & Imine, H. (27–30 April 2020). *Modeling and simulation of bicycle dynamics*. TRA 2020, the 8th Transportation Research Arena, Helsinki, Finland.
31. Shoman, M., & Imine, H. (18–22 October 2020). *Subjective validity of bicycle simulators*. VEHICULAR 2020: The Ninth International Conference on Advances in Vehicular Systems, Technologies and Applications, Porto, Portugal.
32. Shoman, M. M., & Imine, H. (2021). Bicycle simulator improvement and validation. *IEEE Access*, *9*, 55063–55076. https://doi.org/10.1109/ACCESS.2021.3071214